ChemPubSoc Europe
DOI: 10.1002/cssc.201802566
CHEMSUSCHEM
Full Papers

Atomic Layer Deposition of Space-Efficient SnO_2 Underlayers for $BiVO_4$ Host–Guest Architectures for Photoassisted Water Splitting

Benjamin Lamm,[a] Lite Zhou,[b] Pratap Rao,[b] and Morgan Stefik*[a]

Bismuth vanadate ($BiVO_4$) is promising for solar-assisted water splitting. The performance of $BiVO_4$ is limited by charge separation for >70 nm films or by light harvesting for <700 nm films. To resolve this mismatch, host–guest architectures use thin film coatings on 3D scaffolds. Recombination, however, is exacerbated at the extended host–guest interface. Underlayers are used to limit this recombination with a host-underlayer-guest series. Such underlayers consume precious pore volume where typical SnO_2 underlayers are optimized with 65–80 nm. In this study, conformal and ultrathin SnO_2 underlayers with low defect density are produced by atomic layer deposition (ALD). This shifts the optimized thickness to just 8 nm with significantly improved space efficiency. The materials chemistry thus determines the dimension optimization. Lastly, host–guest architectures are shown to have an applied bias photon-to-charge efficiency of 0.71%, a new record for a photoanode absorber prepared by ALD.

Introduction

Bismuth vanadate has for the past decade been studied as a photoanode for photoelectrochemical (PEC) water splitting,[1] with continuous performance gains over time.[2–11] The monoclinic scheelite phase (m-$BiVO_4$) is the highest efficiency allotrope, with a conduction band edge near 0 V vs. the reversible hydrogen electrode (RHE). The valence band edge is near 2.4 V vs. RHE and the band gap is 2.4 eV.[2,12,13] This band alignment provides holes in the valence band with excess potential to photo-oxidize water (1.23 V vs. RHE), whereas electrons have a potential almost suitable for hydrogen evolution (0 V vs. RHE), requiring mild external bias.

Bismuth vanadate requires an optical thickness of approximately 700 nm for efficient light harvesting that is much larger than the sum of the limiting carrier diffusion length and the depletion width.[5,13,14] Electron transport is generally cited as the limiting carrier for charge separation with a transport length of approximately 70 nm.[5,13,14] This combination of characteristics makes solid, compact $BiVO_4$ films inherently inefficient. In contrast, the "host–guest" approach (Figure 1 c) decouples this mismatch of carrier transport from optical absorption by using $BiVO_4$ thin films ("guest") upon a transparent, conductive scaffold ("host").[3,8,10] This approach is sometimes called "extremely thin absorber" (ETA).[3,15–18] Recombination is, however, exacerbated with such high surface area devices where carriers are generated in close proximity to recombination sites at the host–guest interface (Figure 1 a). A well-known method to mitigate recombination at such interfaces is to use an underlayer to block minority carriers (Figure 1 b). For n-type

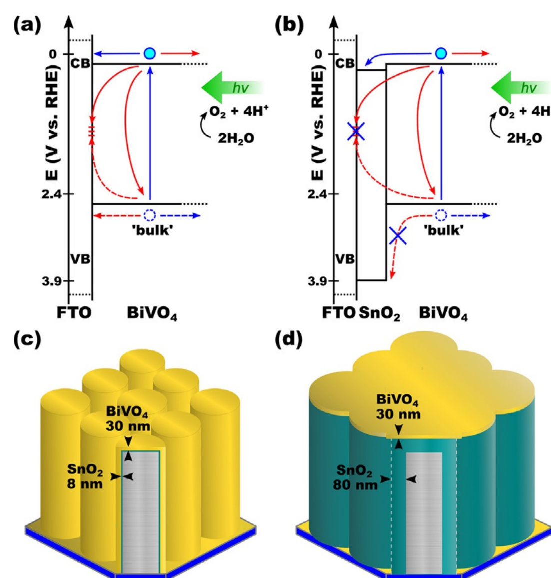

Figure 1. Recombination at the FTO interface with $BiVO_4$ (a) is mitigated by addition of an underlayer composed of SnO_2 (b). The importance of a space-efficient underlayer is shown graphically where limited pore dimensions are only compatible with space-efficient underlayers (c), whereas typical thicker underlayers would fully occupy the free pore volume, preventing realization of a host–guest architecture (d). $BiVO_4$ is drawn as yellow, SnO_2 as teal, and ATO nanowires are gray.

[a] B. Lamm, Dr. M. Stefik
Department of Chemistry and Biochemistry
University of South Carolina, Columbia, SC 29201 (USA)
E-mail: morgan@stefikgroup.com

[b] L. Zhou, Dr. P. Rao
Department of Materials Science and Engineering
Worcester Polytechnic Institute, Worcester, MA 01609 (USA)

Supporting information and the ORCID identification number(s) for the author(s) of this article can be found under:
https://doi.org/10.1002/cssc.201802566.

This publication is part of a Special Issue focusing on "Water Splitting: From Theory to Practice".
Please visit the issue at http://doi.org/10.1002/cssc.v12.9.

© 2019 Wiley-VCH Verlag GmbH & Co. KGaA, Weinheim

materials like $BiVO_4$, the underlayer is sometimes called a hole blocking layer or a "hole mirror."[6,19–25] Previous works have commonly utilized tin oxide (SnO_2)[2,14,29–32,19,21–23,25–28] and tungsten oxide (WO_3),[3,26,33] where SnO_2 is perhaps the most studied underlayer material for $BiVO_4$. Other materials that have been used as interfacial layers in $BiVO_4$ photoanodes include TiO_2,[34,35] Lu_2O_3,[20] and GaO_xN_{1-x};[36] SnO_2 was selected for this study based on its suitable band alignment relative to $BiVO_4$, stability, low cost, and as-yet unexplored investigation as a $BiVO_4$ underlayer using atomic layer deposition (ALD). Popular synthetic methods for SnO_2, such as spray pyrolysis, yield optimal PEC performance with 65–80 nm of underlayer thickness.[2,21] With such a large film thickness, clearly more is at play than rectification. The optimal underlayer will (1) fully cover the host interface, preventing access to recombination sites located in the FTO, (2) not provide a new set of defects that promote recombination, and (3) have minimal thickness to limit the resistance for electron transport to the electrical contact. The optimal underlayer thickness for different synthesis routes is of minor importance for flat compact films; however, it poses a significant limitation for practical use in 3D host–guest architectures with limited free-volume. Consider a design with 30 nm $BiVO_4$, 80 nm SnO_2, and a 3D porous host—it would require a 270 nm pore diameter to accommodate such a coating while leaving behind a nominal 30 nm final pore size. Such thick underlayers thus limit host–guest implementation by requiring large feature sizes that impose a poor balance of roughness factor to the out-of-plane transport length. Furthermore, such a scenario would require >50 vol.% of nonphotoactive material. The consequences of such space- and material-inefficient designs are shown schematically in Figure 1 c, d. There are clear and significant benefits for the rational development of space-efficient underlayers.

Here we examine the efficacy of conformal and low carrier density SnO_2 thin films prepared by ALD as underlayers for $BiVO_4$ PEC films. The use of an ALD synthesis method enables an optimized PEC performance with just an 8 nm underlayer. This result highlights the role of conformal character and minimal carrier density (i.e., low defect density) upon developing space-efficient underlayers. Finally, we demonstrate enhanced performance for host–guest architectures built upon antimony-doped tin oxide (ATO) supports with a 0.71% applied bias proton-to-charge efficiency (ABPE) and a 3.7-fold improved photocurrent at 1.23 V vs. RHE as compared to the analogous flat film design.

Results and Discussion

Photogenerated holes within $BiVO_4$ would ideally all react at the water interface, producing solar fuel. However, holes generated in $BiVO_4$ near the electron-rich FTO can undergo recombination and reduce the quantum efficiency. FTO–absorber interfaces are known to broadly promote recombination for diverse PEC materials,[19,37–41] suggesting that the defects from deliberate fluorine incorporation are recombination sites. Previous reports utilized undoped SnO_2 as an underlayer for $BiVO_4$ where optimal thicknesses were approximately 80 nm,[2,21] and thinner SnO_2 underlayers did not efficiently inhibit recombination. Common synthetic routes for SnO_2, such as spray pyrolysis, result in nonconformal underlayers with relatively high carrier concentrations (10^{19}–10^{21} cm^{-3}; see the Supporting Information, Table S1). These high carrier concentrations perhaps are a result of using $SnCl_4$, resulting in halide defects similar to FTO and high free-carrier densities. We hypothesize that space-efficient underlayers will require conformal coating techniques with low defect density. SnO_2 produced by well-known ALD protocols yields an ideal candidate to test this hypothesis with a conformal deposition technique that results in an order of magnitude reduced carrier density (Table S1).[42,43] The free carriers in SnO_2 come from multiple candidate defects, including oxygen vacancies, tin interstitials, and extrinsic dopants such as Sb^{5+}, F^-, and Cl^-.[44,45] Although these defects improve conductivity in SnO_2, they are also possible recombination sites for PEC devices. Here, the use of a halide-free SnO_2 precursor (TDMASn) prevents halide doping[44,45] while the use of a strong oxidizing agent (ozone) suppresses the formation of oxygen vacancies, thus avoiding several of the candidate recombination centers. ALD also has the advantage of being a self-limiting deposition technique that facilitates conformal surface coatings within 3D porous substrates having a high roughness factor.[42,43,46]

PEC performance vs. SnO_2 thickness

Looking towards space-efficient underlayers, we examined the efficacy of thin 2–32 nm SnO_2 underlayers with low defect density prepared by ALD. With a SnO_2 growth rate of 0.692 Å per cycle, this corresponds to samples made by using 30–480 SnO_2 cycles of (TDMASn–O_3)$_x$; where sample names and corresponding characteristics are described in Table 1. The inclusion of an SnO_2 underlayer had no observed effect on the $BiVO_4$ crystal

Table 1. Flat sample nomenclature and synthesis descriptions.

Name	Substrate	SnO_2 cycles [#]	SnO_2 thickness [nm]	$BiVO_4$ cycles [#]	$BiVO_4$ thickness [nm]
Flat-BV	TEC-15 FTO	0	0	4000	30
Flat-T2-BV	TEC-15 FTO	30	2	4000	30
Flat-T4-BV	TEC-15 FTO	60	4	4000	30
Flat-T8-BV	TEC-15 FTO	120	8	4000	30
Flat-T16-BV	TEC-15 FTO	240	16	4000	30
Flat-T32-BV	TEC-15 FTO	480	32	4000	30

© 2019 Wiley-VCH Verlag GmbH & Co. KGaA, Weinheim

structure, as measured by grazing-incidence wide angle X-ray scattering (GIWAXS; Figure 2a). The only GIWAXS changes noted here are the increased intensity of peaks indexed to tetragonal SnO_2 (cassiterite), corresponding to an increasing SnO_2 thickness. Additionally, the SnO_2 underlayer had no apparent

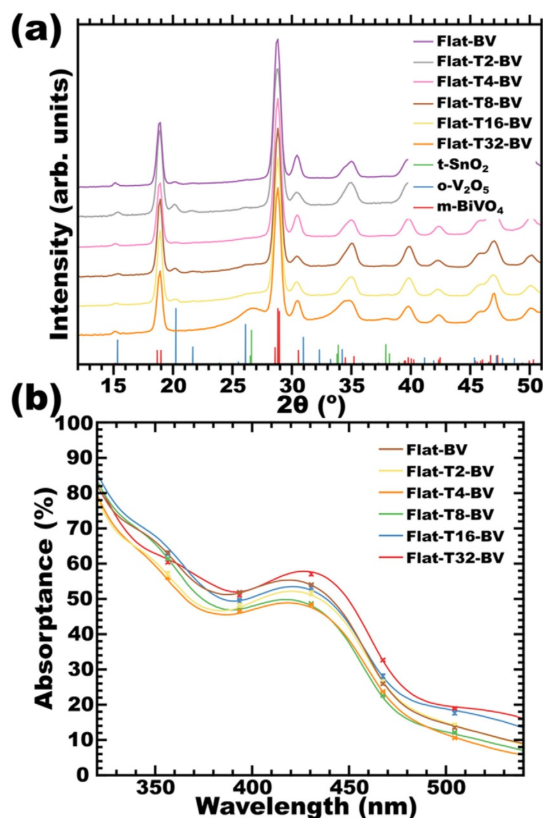

Figure 2. GIWAXS measurements of flat $BiVO_4$ samples with and without underlayers (a), as well as the corresponding UV/Vis absorption spectra (b).

effect on UV/Vis absorption in the measured wavelength range, regardless of underlayer thickness (Figure 2b). Here the UV absorption by the FTO-coated substrates obscures the absorption of such thin ALD SnO_2 films. Consistent with prior reports,[5,7] the growth of $BiVO_4$ by surface-functionalized ALD (SF-ALD) resulted in conformal films (Figure 3). The growth rate here was determined by SEM to be 0.0746 Å per cycle when grown upon FTO or SnO_2.

The charge separation efficiency (φ_{sep}) was measured as a function of the ALD SnO_2 underlayer thickness. Here, the PEC performance was measured in the presence of a hole-scavenging sulfite electrolyte to pin the charge injection efficiency at nearly 100% ($\varphi_{inj} \approx 1$). Thus, the measured photocurrents represent the product of the light-harvesting efficiency (LHE) and the voltage-dependent φ_{sep} [Eqs. (1) and (2)]:[47,48]

$$J_{H_2O}(V) = J_{abs} \times \phi_{sep}(V) \times \phi_{inj}(V) \quad (1)$$

$$J_{sulfite}(V) = J_{abs} \times \phi_{sep}(V) \quad (2)$$

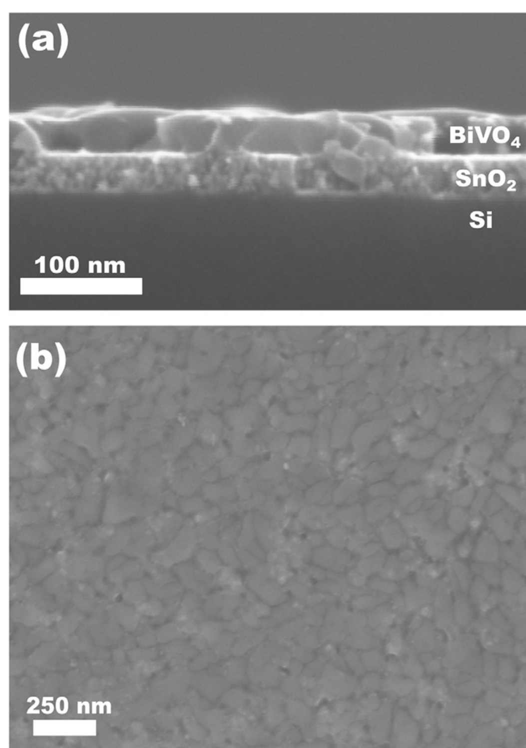

Figure 3. SEM images of sample Flat-T32-BV on Si in cross-section (a) and of sample Flat-T8-BV on FTO from top view (b).

Where J_{abs} is the photon absorption rate expressed as a current density (determined by the illumination spectra and LHE). The SnO_2 underlayers absorbed little light since SnO_2 is a wide band-gap material ($E_g \approx 3.6$–4.0 V)[46,49–51] and used here as very thin layers. Thus, with constant $BiVO_4$ film thickness (constant LHE and J_{abs}) the improvements to photocurrent were attributed solely to improvements to φ_{sep} by reducing the rate of interfacial charge recombination. Complete *J*–*V* curves for this sample series are shown in Figure 4a. For the sake of brevity, we focus the discussion on the most important regime of performance under low applied bias voltage. Sample Flat-BV (without underlayer) gave a photocurrent of 0.19 mA cm^{-2} at 0.7 V vs. RHE, corresponding to $\varphi_{sep} = 6.9\%$ (Figure 4b). The addition of a SnO_2 underlayer significantly improved the photocurrent and φ_{sep} monotonically until a performance maximum was reached with an 8 nm thick SnO_2 underlayer. This sample (denoted Flat-T8-BV) gave a photocurrent of 0.41 mA cm^{-2} at 0.7 V vs. RHE, corresponding to $\varphi_{sep} = 15.1\%$. This represents a 2.2-fold improvement in performance attributed to improved charge separation efficiency with deployment of an optimized underlayer. Samples with yet thicker underlayers, for example, 16 or 32 nm, exhibited diminished performance, attributed to the ohmic resistance of the undoped SnO_2. This is especially evident in the performance of electrodes with a 32 nm SnO_2 underlayer, where PEC performance is reduced to well below that of Flat-BV across most potentials. The thickness trend here is in stark contrast to other reported SnO_2 underlayers that do not exhibit a maximum in performance until a total thickness of approximately 80 nm. We

© 2019 Wiley-VCH Verlag GmbH & Co. KGaA, Weinheim

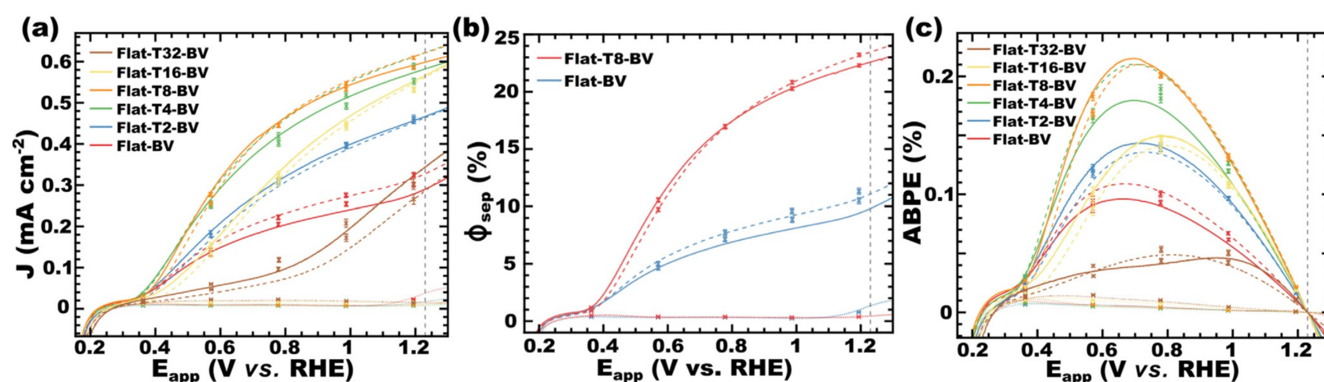

Figure 4. Flat $BiVO_4$ PEC performance was measured with different ALD SnO_2 underlayer thicknesses. The photocurrent (a), φ_{sep} (b), and ABPE (c) were measured. The electrolyte was 1.0 M potassium borate with 0.2 M Na_2SO_3 as a hole scavenger with a pH of 9.36. Simulated AM 1.5G sunlight was used for illuminated measurements. The dark current (dotted), photocurrent with backside illumination (dashed), and photocurrent with frontside illumination (solid) are presented.

attribute the difference for ALD SnO_2 to the improved film conformality and the reduced defect concentration evidenced by the low free carrier concentration (Table S1). The lower performance of very thin films presented herein (i.e., 2 and 4 nm SnO_2) could have several causes: (1) there may be pinholes at the early nucleation stage (island growth) of ALD until a conformal layer is established, (2) the crystallization of amorphous ALD SnO_2 may induce pinhole formation for very thin films (SEM images evidence such roughness from the crystallization process; Figure S1), and (3) fluorine diffusion from the FTO substrate can induce recombination centers in very thin SnO_2 films. Such diffusion of fluorine into SnO_2 is reported to have a negligible spatial extent for the thermal conditions used here.[52] These performance trends with underlayer thickness were also apparent in the applied bias photon-to-charge efficiencies [defined by Eq. (S1)][6] in Figure 4c. Here the maximum performance was found for sample Flat-T8-BV with an ABPE of 0.213% at 0.7 V vs. RHE as compared to just 0.10% for Flat-BV. An optimal of all performance metrics was found for the 8 nm thick ALD SnO_2, thick enough to suppress recombination and thin enough to avoid excessive resistance.

PEC performance of host–guest ATO-NTs/SnO_2/$BiVO_4$

The optimized ALD underlayers were applied towards host–guest nanostructures to enhance the photocurrent response. Many previous studies have used cathodic electrodeposition of $BiVO_4$ or precursors thereof.[3,4,13,53–56] The application of cathodic currents is perhaps challenging subsequent to deposition of an underlayer intended to block holes. In contrast, ALD is capable of conformal depositions regardless of the electronic structure of any preceding layers. Our recently developed SF-ALD of $BiVO_4$ is uniquely suited to enable host–guest strategies that include underlayers. A series of 3D nanostructured transparent conductors were used as hosts for the SF-ALD of 30 nm films of $BiVO_4$. The hosts were composed of antimony-doped tin oxide nanotubes (ATO-NTs) prepared by hydrothermal growth and solution deposition, which had variable lengths of 2.2–2.8 μm.

Host–guest nanostructures were prepared with and without use of SnO_2 underlayers (Table 2). SEM images of the resulting host–guest nanostructures are shown in Figures 5 and 6. The SF-ALD of $BiVO_4$ appeared to reach the bottom of the ATO films where there was considerable roughness from the ATO nanotube synthesis. The expected $BiVO_4$ thickness of 30 nm was visible with nanotube cross-sections after cleaving the tops of the nanotubes (Figure 6). The $BiVO_4$ had some porosity as a result of densification and perhaps loss of residual organics during calcination. The PEC performance was investigated as a function of the prepared architectures. Comparison of host–guest sample ATO2.2-BV (without underlayer) to the corresponding compact Flat-BV sample exhibited a photocurrent of 0.81 vs. 0.20 $mA\,cm^{-2}$ at 0.7 V vs. RHE, a 4.0x increase in performance. Here the use of a host–guest architecture increased the light-harvesting efficiency as expected, where the optical thickness was increased by a factor of around 17 (Table 2). In contrast, the 30 nm thick Flat-BV sample only absorbed 15% of light with 500 nm wavelength (Figure 2b). The addition of

Table 2. 3D host–guest sample nomenclature and synthesis descriptions.

Name	ATO-NT length [μm]	SnO_2 cycles [#]	SnO_2 thickness [nm]	$BiVO_4$ cycles [#]	$BiVO_4$ thickness [nm]	Roughness factor[a]	Optical thickness [nm][a]
ATO2.2-BV	2.2	0	0	4000	30	15.4	527.9
ATO2.2-T8-BV	2.2	120	8	4000	30	15.4	562.4
ATO2.8-T8-BV	2.8	120	8	4000	30	19.4	707.6

[a] Calculated from a simplified geometric estimate (see the Supporting Information for further details).

© 2019 Wiley-VCH Verlag GmbH & Co. KGaA, Weinheim

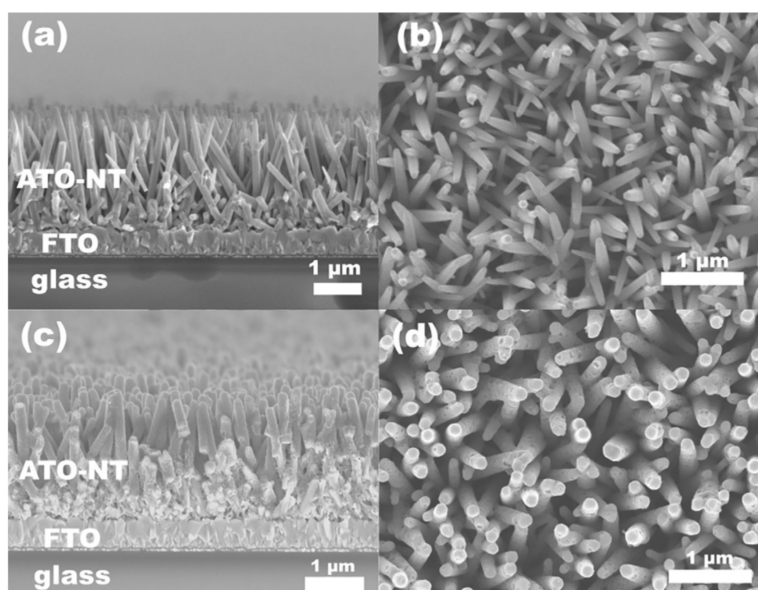

Figure 5. SEM images of ATO-NTs before (a, b) and after $BiVO_4$ SF-ALD (c, d). Sample ATO2.2-T8-BV is shown in panels c and d.

ATO2.2-BV having the same architecture without an underlayer. This difference in performance for $BiVO_4$ deposited on undoped ALD SnO_2 versus that on ATO again suggests the effect of free-carrier-producing defects on enhancing interfacial recombination.

With the beneficial effect of an underlayer demonstrated for these host–guest architectures, we next sought to optimize the light-harvesting efficiency. A series of samples were compared with increasing nanotube length: ATO2.2-T8-BV and ATO2.8-T8-BV. The photocurrent response was nearly identical with a peak photocurrent of 2.1 mA cm^{-2} at 1.23 V vs. RHE (Figure 7 a). Comparing the estimated optical thickness for these two samples indicates that both are rather close to the ideal dimension of 700 nm for efficient light harvesting of 90 % of the below-band gap AM 1.5G spectrum.[6] The lack of an effect of nanotube length and thus of optical thickness here suggests that light-harvesting efficiency is not the limiting factor here, but rather the bulk recombination rate of SF-ALD $BiVO_4$. Further improvements to this performance would thus require new develop-

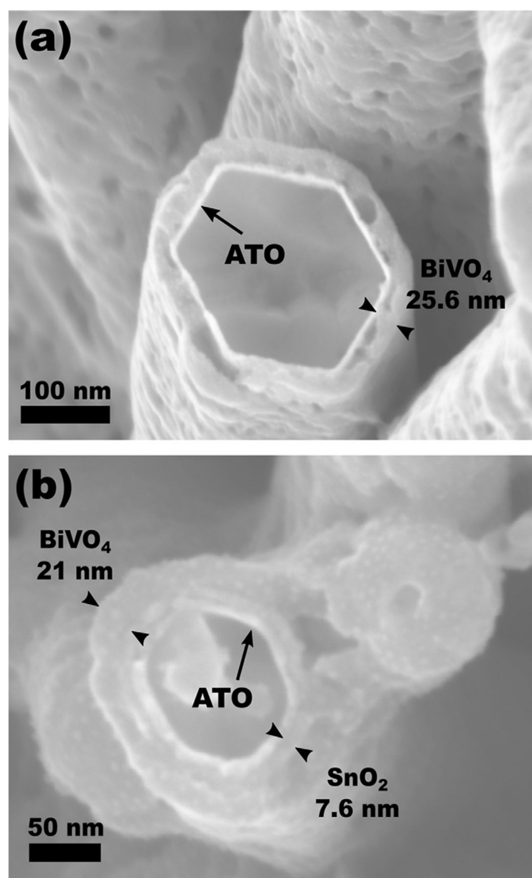

Figure 6. Top-view SEM images of samples ATO2.2-BV (a) and ATO2.2-T8-BV (b) after light abrasion to break open nanotubes.

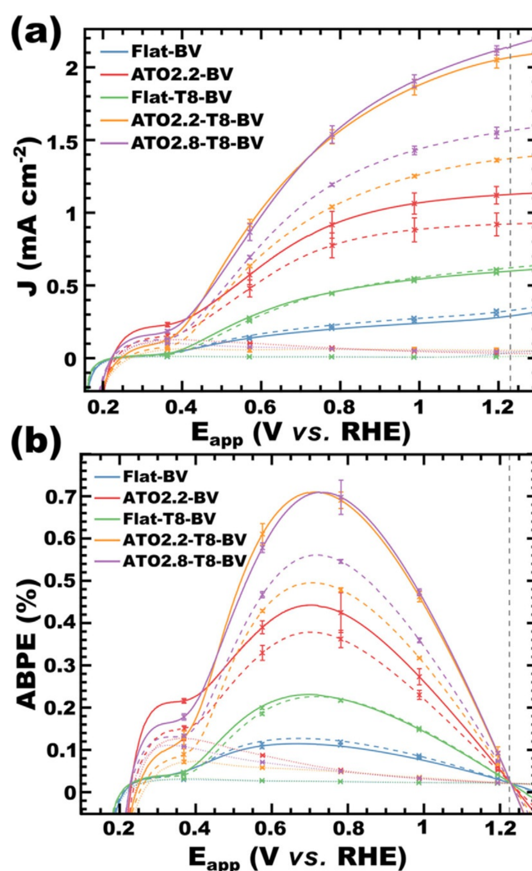

Figure 7. Host–guest PEC performance was measured with and without the optimized underlayer and as a function of nanotube length. The photocurrent (a) and ABPE (b) were measured. The electrolyte was 1.0 M potassium borate with 0.2 M Na_2SO_3 as hole scavenger with a pH of 9.36. Simulated AM 1.5G sunlight was used for illuminated measurements. The dark current (dotted), photocurrent with backside illumination (dashed), and photocurrent with frontside illumination (solid) are presented.

the optimized underlayer was found to significantly increase PEC performance. Sample ATO2.2-T8-BV yielded a photocurrent 1.33 mA cm^{-2} at 0.7 V vs. RHE, which is 1.6 times that with

© 2019 Wiley-VCH Verlag GmbH & Co. KGaA, Weinheim

ments to manage bulk defect chemistry within $BiVO_4$.[6,17,57–59] The ABPEs were calculated for all host–guest structures investigated with a maximum in performance for samples ATO2.2-T8-BV and ATO2.8-T8-BV, which gave 0.71% ABPE at 0.71 V vs. RHE (Figure 7b). These results highlight the advantage of including a space-efficient hole-blocking underlayer within 3D host–guest nanostructures.

The applied bias photon-to-charge efficiency is one of the most important metrics for PEC device performance, as it includes the energetic cost of the applied bias.[6] The performances of PEC devices in which the photoabsorber was prepared by ALD have often been lower than for those used other synthetic methodologies. In light of these challenges, it is insightful to compare the performance here to other ALD-derived PEC photoanodes. The 0.71% ABPE for sample ATO2.2-T8-BV represents, to our knowledge, the highest reported PEC performance of any photoanode material produced by ALD (Table 3). Interestingly, sample Flat-T8-BV is also the highest performing compact film produced by ALD, highlighting that careful underlayer design is crucial for general performance improvements.

Table 3. PEC performance of photoanodes with absorber produced by ALD.

Material	ABPE [%]	Photocurrent[a] [mA cm^{-2}]
$BiVO_4$ (ATO2.2-T8-BV)	0.71	2.1
WO_3 (host–guest)[60]	0.62	2.1
$BiVO_4$ (Flat-T8-BV)	0.213	0.62
$CuWO_4$ (compact)[61]	0.12	1.1
α-Fe_2O_3 (host–guest)[62]	0.091	1.5
Ta_3N_5 (compact)[63]	0.095	0.79
α-Fe_2O_3 (compact)[64]	0.023	0.32

[a] At 1.23 V vs. RHE.

Conclusions

Bismuth vanadate requires an optical thickness of approximately 700 nm for efficient light harvesting and that is much larger than the limiting carrier transport length of 70 nm.[5,13,14] The host–guest approach decouples this mismatch of carrier transport from optical absorption;[3,8,10] however, recombination at the host–guest interface is exacerbated with such high surface area devices. Tin oxide is a popular underlayer material for $BiVO_4$, acting as a hole-blocking layer typically optimized at 65–80 nm.[2,21] Such thick underlayers, however, consume precious pore volume from the overall 3D host–guest design. The efficacy of low carrier density SnO_2 underlayers were investigated for $BiVO_4$ PEC performance. The use of an ALD synthesis method resulted in more conformal coatings with lower defect densities and enabled optimized PEC performance with only an 8 nm underlayer. Such thin underlayers yield considerably improved space-efficiency for deployment within reasonable host–guest architectures. The materials chemistry was shown to influence the underlayer thickness optimization. Host–guest architectures built upon ATO nanotubes were demonstrated. SnO_2 underlayers improved the performance where an overall 3.7-fold improved photocurrent was feasible at 1.23 V vs. RHE.

Experimental Methods

Materials

Tetrakis(dimethylamino) tin (TDMASn, 99%), triphenyl bismuth ($BiPh_3$, 99%), and vanadium(V) oxytriisopropoxide (VTIP, 98%) were used as received from STREM. Deionized ultra-filtered (DIUF) water (Fisher), methanol (ACS Grade, Fisher), 2-propanol (70% lab grade, BDH), H_3BO_3 (ACS Grade, VWR Life Science), Na_2SO_3 (ACS Grade, Macron), and KOH (ACS Grade, Fisher) were used as received. TEC-15 fluorine-doped tin oxide (FTO)-coated glass was purchased from Hartford Glass. The FTO substrates were cleaned extensively before use with 2-propanol and DIUF water before sonication in soapy water (Decon Contrex, 2 wt%), followed by additional rinses with water and 2-propanol, followed by sonication in 2-propanol. Polished n-doped silicon wafers with (100) orientation were purchased from University Wafers, USA. The cleaned FTO substrates and silicon wafers were calcined by using a Barnstead Thermolyne muffle furnace at 450 °C for 1 h immediately prior to deposition. High-temperature grade Kapton tape was purchased from McMaster-Carr, USA. Ultra-high purity nitrogen (99.999%) and oxygen (99.5%) were used as received from Praxair.

ATO nanotube synthesis

The hydrothermal growth of the ZnO nanorod array (NRA) template was adapted from previously reported methods.[10,65,66] Arrays of ZnO nanowires were synthesized on 3×3 cm^2 FTO substrates that were cleaned thoroughly by sonication in acetone, isopropyl alcohol, and deionized water before coating with a seed layer (5 mM acetate dihydrate in ethanol) by spin coating at 2000 rpm for 30 s. Samples with seed layer were annealed at 350 °C for 30 min.

ZnO nanowires were grown by immersing seeded substrates in aqueous solutions containing 25 mM zinc nitrate hexahydrate (98%, Sigma Aldrich) and 25 mM hexamethylenetetramine (99%, Sigma Aldrich) at 90–95 °C for 1 and 2 h. To obtain longer nanowire arrays, the substrates grown for 1 and 2 h were introduced to fresh solution (20 mM zinc nitrate hydrate and 20 mM hexamethylenetetramine) and grown for an additional 2 h. The total growth time for the two types of samples were 2 h and 3 h (1 h followed by 2 h).

The Sb:SnO_2 nanotube arrays were synthesized by coating Sb:SnO_2 layers onto the ZnO nanowires template. A Sb:SnO_2 solution containing $SnCl_2$ (0.1225 g, 98%, Sigma Aldrich) and $SbCl_3$ (0.01 g, 99%, Sigma Aldrich) in 2-methoxyethanol (10 mL, 99%, Alfa Aesar) was drop cast onto the ZnO nanowire templates. After four layers of Sb:SnO_2 coating, the substrates were annealed in a furnace in air at 550 °C for 2 h to crystallize the Sb:SnO_2 nanotube shell. Then, the ZnO nanowires template with the Sb:SnO_2 shell was etched in acetic acid (99.7%, Sigma Aldrich) for 2 h and thoroughly washed in deionized water to remove the ZnO nanowires template from the substrates. After first-time growth, substrates were again repeatedly drop cast with Sb:SnO_2 solution, annealed in a furnace, and etched in acetic acid one more time to make the Sb:SnO_2 nanotube arrays with thicker walls.

© 2019 Wiley-VCH Verlag GmbH & Co. KGaA, Weinheim

Atomic layer deposition of tin oxide and bismuth vanadate films

Samples were masked by using Kapton tape to define the deposition region on the back and partially on the front to provide clean electrical contacts for PEC measurements. TDMASn was loaded into a stainless steel cylinder in an argon glovebox. The cylinders were sealed and connected to an Arradiance Gemstar-8 reactor. Nitrogen was used as both the carrier gas and the purging gas. A Nano ozone generator (Absolute Ozone, Canada) was used to supply around 10 wt% ozone. The ozone generator was primed with flowing O_2 prior to deposition. Nitrogen was used as both the carrier gas and the purging gas. Precursor dosing was controlled by using Swagelok ALD valves. The TDMASn was heated to 55 °C. The oxidant and precursor manifolds were heated to 100 and 130 °C, respectively. The reactor chamber was set to 115 °C. The TDMASn and ozone had pulse times of 1500 and 100 ms, respectively. The reactor chamber was isolated before each pulse to contain the precursors for 1 s after exposure ("exposure mode"). Excess precursors were purged after each exposure with 200 sccm nitrogen for 10 s. The deposition was organized into a macrocycle of $(\text{TDMASn–O}_3)_a$ where a controlled the total thickness deposited. Tin oxide films on silicon wafers and FTO were calcined prior to bismuth vanadate deposition. A comprehensive ALD protocol is provided in Table S2.

Bismuth vanadate deposition was carried out by using a previously reported SF-ALD procedure,[5] following the original ALD bismuth vanadate demonstration.[7] The $BiPh_3$ and VTIP cylinders were heated to 130 and 45 °C, respectively. The reactor manifolds and chamber were set to 130 °C. Both metal precursors had a pulse time of 2 s, methanol had a pulse time of 50 ms, and water had a pulse time of 25 ms prior to methanol and 100 ms prior to $BiPh_3$. A vapor-boosting 20 ms pulse of nitrogen was added to the $BiPh_3$ cylinder just prior to each pulse. The reactor was isolated in exposure mode for 1 s. Excess precursors were purged after each exposure using 200 sccm nitrogen for 10 s. The deposition was organized into a macrocycle of $(\text{methanol/VTIP/water/BiPh}_3\text{/water})_b$ where methanol was used to control composition and b controlled the total thickness deposited; a comprehensive ALD protocol is given in Table S3.

Film treatments

The ALD films were heated to induce crystallization. Samples were heated at 5 °C min^{-1} to 200 °C, followed by 10 °C min^{-1} to 450 °C, held constant at 450 °C for 1 h, and allowed to cool in the furnace.

Prior to linear sweep voltammetry (LSV), chronoamperometry (CA), and absorptance measurements, films on FTO were exposed to an external bias of 0.6 V vs. RHE (−0.153 V vs. Ag/AgCl at pH 9.36) under AM 1.5G illumination for 1 h (termed PEC activation).[5,6] Films on ATO NTs were exposed to an identical procedure for 2 h.

Diffraction

X-ray diffraction experiments were conducted by using a SAXSLab Ganesha at the South Carolina SAXS Collaborative. A Xenocs GeniX 3D microfocus source was used with a Cu target to generate a monochromatic beam with a 0.154 nm wavelength. The instrument was calibrated by using silicon powder (NIST 640d). Scattering data were processed from the scattering vector $q = 4\pi\lambda^{-1}\sin\theta$ where λ is the X-ray wavelength and 2θ is the total scattering angle. A Pilatus 300 K detector (Dectris) was used to collect the two-dimensional (2D) scattering patterns. Samples were measured with the beam at an incident angle of 8° relative to the film plane. SAXSGUI software was used to radially integrate the 2D patterns to produce 1D profiles.

Photoelectrochemical and electrochemical measurements

LSVs were measured using a three-electrode potentiostat (BioLogic SP-150) with a Ag/AgCl/KCl (saturated) reference electrode (Pine Instruments) and a platinum wire counter electrode (Pine Instruments). Samples on FTO substrates were clamped with a titanium sheet to provide an ohmic contact. The electrodes were placed into a cell made of polyether ether ketone (PEEK) with a fused-silica window. Simulated sunlight was generated using a 75 W xenon arc lamp (OBB, Horiba) that passed through a water infrared filter (OBB, Horiba), a KG-3 filter (317–710 nm pass, Edmund Optics), and a BG-40 filter with an antireflective coating (335–610 nm pass, Thorlabs). This combination of filters removed much of the UV light where the Xe lamp has the most spectral mismatch from the AM 1.5G spectrum. The transmitted light was collimated by using a fused-silica lens (Thorlabs) and passed through an engineered diffuser with a top-hat profile to provide a homogenous intensity profile with a slight 10° divergence. The transmitted light was corrected for brightness in the 335–610 nm spectral range to generate a photocurrent identical to AM 1.5G sunlight. The illumination intensity was measured by using a calibrated UV-enhanced silicon photodiode (Thorlabs) equipped with a neutral reflective filter (optical density 1.0, Thorlabs) to maintain a linear and calibrated photodiode response. This calibration practice provides accurate solar simulation in terms of both spectral distribution and brightness with a minimal correction factor.[67] PEC measurements were performed in 1 M potassium borate with 0.2 M sodium sulfite (Na_2SO_3) as hole scavenger at pH 9.35. It has been well established that potassium phosphate buffers dissolve $BiVO_4$ at working pH values;[4,68,69] however, $BiVO_4$ photoanodes are stable in alkaline borate buffers. The potassium borate solution was prepared by adjusting the pH of 1 M H_3BO_3 in DIUF water to 9.35 ± 0.02 with KOH as confirmed by a calibrated Thermo Scientific OrionStar A211 pH meter. The sulfite acted as a hole scavenge to provide quantitative charge injection from the semiconductor to the electrolyte for the measurement of film performance without catalysts. The samples were scanned from −0.600 to 0.650 V vs. Ag/AgCl reference electrode at 10 mV s^{-1}. Multiple scans were completed at each condition to confirm reproducibility and the second scan results were reported. For host–guest samples on ATO nanotubes, N_2 sparging was used during all PEC measurements to circulate the electrolyte and dislodge gas bubbles trapped at the surface.

Quantum efficiencies were calculated based on chronoamperometry (CA) measurements made with monochromatic light while using the same potassium phosphate buffer described above. Illumination was generated by using a 150 W xenon lamp (OBB, Horiba) that passed through an 180° monochromator with a 5 mm slit width and 1200 grates per mm diffraction grating (OBB, Horiba). Transmitted light was collimated using a fused-silica lens (Thorlabs) and passed through an engineered diffusor with a top-hat profile to provide a homogenous intensity profile with a slight 10° divergence. CA measurements were recorded at 0.4784 V vs. Ag/AgCl reference electrode (1.23 V vs. RHE) unless otherwise noted. All electrochemical potentials E were reported versus the reversible hydrogen electrode (RHE) using the formula $E(\text{vs. RHE}) = E(\text{vs. Ag/AgCl}) + E_{ref}(\text{Ag/AgCl}) + 0.059\text{ V} \times \text{pH}$ where $E_{ref} = 0.197$ V in this case.

© 2019 Wiley-VCH Verlag GmbH & Co. KGaA, Weinheim

For both CA and LSV measurements, representative samples of a given set were plotted with the mean (indicated as “x”) and bars for the error of the mean.

Optoelectronic properties

The optical response of thin films was measured by using a Shimadzu UV-2450. A sandwich configuration of FTO-water-fused quartz was used to minimize light scattering differences between the blank measurement of bare FTO and samples coated onto FTO. Identical measurements on FTO were used to establish the baseline for the measurements of the optical properties of the deposited films alone.

Morphology

A Zeiss Ultra Plus scanning electron microscope (SEM) was operated at 5 kV using an in-lens secondary electron detector to observe the film surface and cross-sectional acquisition. ALD growth rates were calculated based on cross-sectional SEM imaging of films in the 20–100 nm thickness range.

Hall effect measurements

Electronic properties were measured by using a Hall probe (MMR Technologies K2500) with 100 nm Al contacts connected by magnetic sputtering to a 500 nm thick SnO_2 sample on quartz. Measurements were made with a 12.5 kG magnetic field and 5.14 nA current. The sample was made by five consecutive 100 nm ALD depositions described above, with heat treatments between each deposition.

Acknowledgements

B.L. and M.S. acknowledge support by the National Science Foundation (DMR-1752615). L.Z. and P.M.R. acknowledge support by the National Science Foundation (DMR-1609538). The authors would like to thank Binod Giri for assistance with Hall effect measurements.

Conflict of interest

The authors declare no conflict of interest.

Keywords: atomic layer deposition · Bismuth vanadate · host–guest · photoelectrochemistry · water splitting

[1] A. Kudo, K. Ueda, H. Kato, I. Mikami, *Catal. Lett.* **1998**, *53*, 229 – 230.
[2] F. F. Abdi, L. Han, A. H. M. Smets, M. Zeman, B. Dam, R. van de Krol, *Nat. Commun.* **2013**, *4*, 2195 – 2202.
[3] Y. Pihosh, I. Turkevych, K. Mawatari, J. Uemura, Y. Kazoe, S. Kosar, K. Makita, T. Sugaya, T. Matsui, D. Fujita, M. Tosa, M. Kondo, T. Kitamori, *Sci. Rep.* **2015**, *5*, 11141.
[4] Y. Kuang, Q. Jia, H. Nishiyama, T. Yamada, A. Kudo, K. Domen, *Adv. Energy Mater.* **2016**, *6*, 1501645.
[5] B. Lamm, A. Sarkar, M. Stefik, *J. Mater. Chem. A* **2017**, *5*, 6060 – 6069.
[6] B. Lamm, B. J. Trześniewski, H. Döscher, W. A. Smith, M. Stefik, *ACS Energy Lett.* **2018**, *3*, 112 – 124.
[7] M. Stefik, *ChemSusChem* **2016**, *9*, 1727 – 1735.
[8] X. Shi, I. Y. Choi, K. Zhang, J. Kwon, D. Y. Kim, J. K. Lee, S. H. Oh, J. K. Kim, J. H. Park, *Nat. Commun.* **2014**, *5*, 4775 – 4783.
[9] K. T. Butler, B. J. Dringoli, L. Zhou, P. M. Rao, A. Walsh, L. V. Titova, *J. Mater. Chem. A* **2016**, *4*, 18516 – 18523.
[10] L. Zhou, Y. Yang, J. Zhang, P. M. Rao, *ACS Appl. Mater. Interfaces* **2017**, *9*, 11356 – 11362.
[11] L. Zhou, C. Zhao, B. Giri, P. Allen, X. Xu, H. Joshi, Y. Fan, L. V. Titova, P. M. Rao, *Nano Lett.* **2016**, *16*, 3463 – 3474.
[12] S. Tokunaga, H. Kato, A. Kudo, *Chem. Mater.* **2001**, *13*, 4624 – 4628.
[13] T. W. Kim, K.-S. K.-S. Choi, *Science* **2014**, *343*, 990 – 994.
[14] F. F. Abdi, R. Van De Krol, *J. Phys. Chem. C* **2012**, *116*, 9398 – 9404.
[15] T. Hisatomi, H. Dotan, M. Stefik, K. Sivula, A. Rothschild, M. Grätzel, N. Mathews, *Adv. Mater.* **2012**, *24*, 2699 – 2702.
[16] K. Sivula, F. Le Formal, M. Grätzel, *ChemSusChem* **2011**, *4*, 432 – 449.
[17] K. Tolod, S. Hernández, N. Russo, *Catalysts* **2017**, *7*, 13.
[18] M. Grätzel, *Nature* **2001**, *414*, 338 – 344.
[19] Y. Liang, T. Tsubota, L. P. A. Mooij, R. van de Krol, *J. Phys. Chem. C* **2011**, *115*, 17594 – 17598.
[20] W. Zhang, D. Yan, X. Tong, M. Liu, *Adv. Funct. Mater.* **2018**, *28*, 1705512.
[21] S. Byun, B. Kim, S. Jeon, B. Shin, *J. Mater. Chem. A* **2017**, *5*, 6905 – 6913.
[22] P. Chatchai, Y. Murakami, S.-Y. Kishioka, A. Y. Nosaka, Y. Nosaka, *Electrochem. Solid-State Lett.* **2008**, *11*, H160 – H163.
[23] E. Alarcón-Lladó, L. Chen, M. Hettick, N. Mashouf, Y. Lin, A. Javey, J. W. Ager, *Phys. Chem. Chem. Phys.* **2014**, *16*, 1651 – 1657.
[24] L. Chen, E. Alarcón-Lladó, M. Hettick, I. D. Sharp, Y. Lin, A. Javey, J. W. Ager, *J. Phys. Chem. C* **2013**, *117*, 21635 – 21642.
[25] S. S. M. Bhat, J. M. Suh, S. Choi, S.-P. Hong, S. A. Lee, C. Kim, C. W. Moon, M. G. Lee, H. W. Jang, *J. Mater. Chem. A* **2018**, *6*, 14633 – 14643.
[26] R. Saito, Y. Miseki, K. Sayama, *Chem. Commun.* **2012**, *48*, 3833.
[27] B. J. Trześniewski, W. A. Smith, *J. Mater. Chem. A* **2016**, *4*, 2919 – 2926.
[28] B. J. Trześniewski, I. A. Digdaya, T. Nagaki, S. Ravishankar, I. Herraiz-Cardona, D. A. Vermaas, A. Longo, S. Gimenez, W. A. Smith, *Energy Environ. Sci.* **2017**, *10*, 1517 – 1529.
[29] Y. Liang, J. Messinger, *Phys. Chem. Chem. Phys.* **2014**, *16*, 12014.
[30] I. D. Sharp, J. K. Cooper, F. M. Toma, R. Buonsanti, *ACS Energy Lett.* **2017**, *2*, 139 – 150.
[31] M. Favaro, F. F. Abdi, M. Lamers, E. J. Crumlin, Z. Liu, R. van de Krol, D. E. Starr, *J. Phys. Chem. B* **2018**, *122*, 801 – 809.
[32] F. F. Abdi, T. J. Savenije, M. M. May, B. Dam, R. van de Krol, *J. Phys. Chem. Lett.* **2013**, *4*, 2752 – 2757.
[33] Y. Pihosh, I. Turkevych, K. Mawatari, T. Asai, T. Hisatomi, J. Uemura, M. Tosa, K. Shimamura, J. Kubota, K. Domen, K. Kitamori, *Small* **2014**, *10*, 3692 – 3699.
[34] H. Zhang, C. Cheng, *ACS Energy Lett.* **2017**, *2*, 813 – 821.
[35] J. Gu, Q. Huang, Y. Yuan, K.-H. Ye, Z. Wang, W. Mai, *J. Mater. Chem. A* **2017**, *5*, 20195 – 20201.
[36] B. K. Kang, G. S. Han, J. H. Baek, D. G. Lee, Y. H. Song, S. B. Kwon, I. S. Cho, H. S. Jung, D. H. Yoon, *Adv. Mater. Interfaces* **2017**, *4*, 1700323.
[37] L. Steier, I. Herraiz-Cardona, S. Gimenez, F. Fabregat-Santiago, J. Bisquert, S. D. Tilley, M. Grätzel, *Adv. Funct. Mater.* **2014**, *24*, 7681 – 7688.
[38] T. Hisatomi, J. Brillet, M. Cornuz, F. Le Formal, N. Tétreault, K. Sivula, M. Grätzel, *Faraday Discuss.* **2012**, *155*, 223 – 232.
[39] M. S. Prévot, Y. Li, N. Guijarro, K. Sivula, *J. Mater. Chem. A* **2016**, *4*, 3018 – 3026.
[40] M. Bärtsch, M. Sarnowska, O. Krysiak, C. Willa, C. Huber, L. Pillatsch, S. Reinhard, M. Niederberger, *ACS Omega* **2017**, *2*, 4531 – 4539.
[41] S. Murcia-López, C. Fàbrega, D. Monllor-Satoca, M. D. Hernández-Alonso, G. Penelas-Pérez, A. Morata, J. R. Morante, T. Andreu, *ACS Appl. Mater. Interfaces* **2016**, *8*, 4076 – 4085.
[42] M. Stefik, M. Cornuz, N. Mathews, T. Hisatomi, S. Mhaisalkar, M. Grätzel, *Nano Lett.* **2012**, *12*, 5431 – 5435.
[43] J. W. Elam, D. A. Baker, A. J. Hryn, A. B. F. Martinson, M. J. Pellin, J. T. Hupp, *J. Vac. Sci. Technol. A* **2008**, *26*, 244.
[44] R. Kykyneshi, J. Zeng, D. P. Cann in *Handbook of Transparent Conductors* (Eds.: D. S. Ginley, H. Hosono, D. C. Paine), Springer, Boston, **2011**, pp. 171 – 191.
[45] J. A. Aboaf, V. C. Marcotte, N. J. Chou, *J. Electrochem. Soc.* **1973**, *120*, 701.
[46] M. N. Mullings, C. Hägglund, S. F. Bent, *J. Vac. Sci. Technol. A* **2013**, *31*, 061503.

© 2019 Wiley-VCH Verlag GmbH & Co. KGaA, Weinheim

[47] H. Dotan, K. Sivula, M. Grätzel, A. Rothschild, S. C. Warren, *Energy Environ. Sci.* **2011**, *4*, 958–964.
[48] D. K. Zhong, S. Choi, D. R. Gamelin, *J. Am. Chem. Soc.* **2011**, *133*, 18370–18377.
[49] M. Batzill, U. Diebold, *Prog. Surf. Sci.* **2005**, *79*, 47–154.
[50] D. Davazoglou, *Thin Solid Films* **1997**, *302*, 204–213.
[51] W. Spence, *J. Appl. Phys.* **1967**, *38*, 3767–3770.
[52] C. F. Wan, R. D. McGrath, W. F. Keenan, Y. S. Tung, S. N. Frank, *J. Electrochem. Soc.* **1988**, *135*, 985.
[53] K. J. McDonald, K.-S. Choi, *Energy Environ. Sci.* **2012**, *5*, 8553.
[54] D. K. Lee, K.-S. Choi, *Nat. Energy* **2018**, *3*, 53–60.
[55] G. V. Govindaraju, G. P. Wheeler, D. Lee, K.-S. Choi, *Chem. Mater.* **2017**, *29*, 355–370.
[56] T. W. Kim, Y. Ping, G. A. Galli, K.-S. Choi, *Nat. Commun.* **2015**, *6*, 8769.
[57] Z. Li, W. Luo, M. Zhang, J. Feng, Z. Zou, *Energy Environ. Sci.* **2013**, *6*, 347–370.
[58] H. L. Tan, R. Amal, Y. H. Ng, *J. Mater. Chem. A* **2017**, *5*, 16498–16521.
[59] Y. Park, K. J. McDonald, K.-S. Choi, *Chem. Soc. Rev.* **2013**, *42*, 2321–2337.
[60] R. Liu, Y. Lin, L.-Y. Chou, S. W. Sheehan, W. He, F. Zhang, H. J. M. Hou, D. Wang, *Angew. Chem. Int. Ed.* **2011**, *50*, 499–502; *Angew. Chem.* **2011**, *123*, 519–522.
[61] Y. Gao, O. Zandi, T. W. Hamann, *J. Mater. Chem. A* **2016**, *4*, 2826–2830.
[62] Y. Lin, S. Zhou, S. W. Sheehan, D. Wang, *J. Am. Chem. Soc.* **2011**, *133*, 2398–2401.
[63] H. Hajibabaei, O. Zandi, T. W. Hamann, *Chem. Sci.* **2016**, *7*, 6760–6767.
[64] L. Steier, J. Luo, M. Schreier, M. T. Mayer, T. Sajavaara, M. Grätzel, *ACS Nano* **2015**, *9*, 11775–11783.
[65] M. Law, L. E. Greene, J. C. Johnson, R. Saykally, P. Yang, *Nat. Mater.* **2005**, *4*, 455–459.
[66] L. E. Greene, M. Law, D. H. Tan, M. Montano, J. Goldberger, G. Somorjai, P. Yang, *Nano Lett.* **2005**, *5*, 1231–1236.
[67] C. H. Seaman, *Sol. Energy* **1982**, *29*, 291–298.
[68] F. M. Toma, J. K. Cooper, V. Kunzelmann, M. T. McDowell, J. Yu, D. M. Larson, N. J. Borys, C. Abelyan, J. W. Beeman, K. M. Yu, J. H. Yang, L. Chen, M. R. Shaner, J. Spurgeon, F. A. Houle, K. A. Persson, I. D. Sharp, *Nat. Commun.* **2016**, *7*, 12012.
[69] T. W. Kim, K.-S. Choi, *J. Phys. Chem. Lett.* **2016**, *7*, 447–451.

Manuscript received: November 7, 2018
Revised manuscript received: December 14, 2018
Accepted manuscript online: December 20, 2018
Version of record online: January 22, 2019

© 2019 Wiley-VCH Verlag GmbH & Co. KGaA, Weinheim